Contrib Mineral Petrol (2016) 171:23
DOI 10.1007/s00410-016-1232-1

ORIGINAL PAPER

Primary cumulus platinum minerals in the Monts de Cristal Complex, Gabon: magmatic microenvironments inferred from high-definition X-ray fluorescence microscopy

Stephen J. Barnes[1] · Louise A. Fisher[1] · Bélinda Godel[1] · Mark A. Pearce[1] · Wolfgang D. Maier[2] · David Paterson[3] · Daryl L. Howard[3] · Christopher G. Ryan[4] · Jamie S. Laird[4]

Received: 18 March 2015 / Accepted: 13 January 2016 / Published online: 25 February 2016

Abstract An unusual occurrence of Pt-enriched pyroxenites in the Monts de Cristal igneous complex is characterized by unusually high ratios of Pt to other platinum-group elements (PGEs) and very low Cu and sulfide contents. Synchrotron X-ray fluorescence microscopy was used to identify over a hundred discrete grains of platinum minerals and relate their occurrence to textural associations in the host heteradcumulate orthopyroxenites. Element associations, backed up by FIB-SEM and PIXE probe observations, indicate that most of the Pt is associated with either As- or trace Cu–Ni-rich sulfides, or both. Some of the Pt–As grains can be identified as sperrylite, and most are likely to be Pt–Fe alloy. The relative abundances and volumes of Pt minerals to sulfide minerals are very large compared with typical magmatic sulfides. Almost all of the grains observed lie at or within a few tens of μm of cumulus orthopyroxene grain boundaries, and there is no significant difference between the populations of grains located inside or outside plagioclase oikocrysts. These oikocrysts are inferred to have crystallized either at the cumulus stage or very shortly thereafter, on the basis of their relationship to Ti enrichment in the margins of pyroxene grains not enclosed in oikocrysts. This relationship precludes a significant role of trapped intercumulus liquid in Pt deposition or mobilization and also allows a confident inference that Pt-rich and Pt–As-enriched phases precipitated directly from the magma at the cumulus stage. These observations lead to the conclusion that fractionation of Pt from other PGEs in this magmatic system is a consequence of a solubility limit for solid Pt metal and/or Pt arsenide.

Keywords Platinum · Cumulates · Layered intrusions · PGEs

Introduction

The platinum-group elements (PGEs) occupy an unusual niche in geochemical studies, in that they are present in the Earth's crust at extremely low levels, but are highly informative tracers of a wide variety of geochemical processes including crust–mantle differentiation (Becker et al. 2006; Lorand et al. 2008; Maier et al. 2009) and ore deposit genesis (Mungall and Naldrett 2008; Fiorentini et al. 2010). For this reason, they are among the few elements routinely analyzed at parts per billion levels in rocks.

Identifying the mineral hosts of PGEs in silicate rocks and sulfide ores is a highly challenging process, commonly involving the examination of dozens or even hundreds of standard petrographic thin sections to identify a handful of grains intersecting the sample surface (Godel et al. 2010; Godel 2013). Scanning X-ray fluorescence microscopy (XFM) using synchrotron radiation has emerged as a powerful technique for rare phase detection, as a result of the penetrating power of synchrotron X-ray radiation and the resulting ability to image small grains within a sample

Communicated by Chris Ballhaus.

Electronic supplementary material The online version of this article (doi:10.1007/s00410-016-1232-1) contains supplementary material, which is available to authorized users.

✉ Stephen J. Barnes
Steve.Barnes@csiro.au

[1] CSIRO Mineral Resources, Perth, Australia

[2] School of Earth and Ocean Sciences, Cardiff University, Cardiff, UK

[3] Australian Synchrotron, Melbourne, Australia

[4] CSIRO Mineral Resources, Melbourne, Australia

volume as opposed to intersecting a surface (Ryan et al. 2014a). The use of synchrotron radiation increases by ~70 times the chance of intersecting rare phases compared to conventional 2D techniques such as SEM (Godel 2013). This technique was employed by Kogiso et al. (2008) to image PGE minerals in samples of mantle peridotite at concentrations of around 25 ppb total PGEs. The use of the Maia multi-detector array in XFM enables this method to be extended to mapping thin polished rock samples over areas of several cm^2 and thicknesses of >100 μm, at dwell times much less (Ryan et al. 2014a, b) than those employed by Kogiso et al. (2008). By this method, Pt minerals less than 5 μm in diameter can be detected in samples containing 10 s of ppb Pt, with scanning times of a few hours per standard sized thin section.

To date, most studies of PGEs in igneous rocks have identified immiscible magmatic sulfide liquid as the predominant phase controlling PGE abundances, as a consequence of the extremely high partition coefficients for PGEs between silicate and sulfide into this phase (Campbell et al. 1983; Fonseca et al. 2009; Mungall and Brenan 2014). However, an increasing body of experimental and geochemical evidence indicates that in certain circumstances, PGE minerals may crystallize directly from silicate magmas, despite the extremely low ppb-level concentrations of PGEs in the silicate magma (Borisov and Palme 1997, 2000; Andrews and Brenan 2002; Barnes and Fiorentini 2008). This principle has been well established for the Ir-series PGEs Ir, Os, and Ru, and direct precipitation of IPGE alloy phases from S-free silicate magma has been demonstrated experimentally (Finnigan et al. 2008), but direct precipitation from magma has yet to be conclusively demonstrated for Pt. Furthermore, recent experimental data (Mungall and Brenan 2014) have demonstrated that small amounts of S in basaltic melts substantially increase the solubilities of PGE alloys compared with the very low values reported in S-free studies (Borisov and Palme 1997, 2000).

Platinum and Pd are typically very strongly correlated in high-temperature magmas such as komatiites (Fiorentini et al. 2011; Barnes and Liu 2012) but tend to diverge in more fractionated basaltic suites, where Pt appears to behave more compatibly; this divergence has been attributed to compatibility of Pt in silicate phases (Keays and Lightfoot 2010; Keays et al. 2012). However, there is no experimental or mineral chemical evidence for significant compatibility of Pt in common igneous silicates. Direct Pt crystallization from island arc magmas is inferred by Park and Campbell (2013) on the basis of magma composition trends, but no Pt-rich mineral phases were identified. A number of studies have identified what appear to be primary platinum-group minerals (PGMs) in sulfide-poor komatiites (Fiorentini et al. 2007; Locmelis et al. 2009), but these are all in hydrothermally altered rocks so a primary origin cannot be conclusively established. Crucial to understanding the magmatic behavior of Pt is the identification of clearly primary, liquidus Pt minerals in igneous cumulate rocks, i.e., in the solid products of fractional crystallization. This identification is complicated by the possibility that PGEs may be concentrated in rocks by initial accumulation of PGE-enriched sulfide liquid, followed by extensive post-cumulus loss of the sulfide component due to dissolution, devolatilization, or oxidation (Naldrett et al. 1989; Fonseca et al. 2012; Wohlgemuth-Ueberwasser et al. 2013), a possibility that is considered in detail below.

Maier et al. (2015) report the identification of primary Pt-rich phases present in fresh cumulate pyroxenites containing anomalous concentrations of Pt, in the range 20–150 ppb, in the Monts de Cristal layered intrusion in Gabon, west Africa. This occurrence is distinctly different from other stratiform PGE concentrations in layered intrusions in that the PGE abundances are dominated by Pt, with very low concentrations of all other PGEs. In this study, we extended the XFM work reported in the previous study, using the Maia detector array on the XFM beamline of the Australian Synchrotron on an additional five samples. The prime objectives were

1. To investigate the detailed elemental associations of the Pt-rich phases, and particularly their association or otherwise with sulfides; and
2. To relate the deposition and possible post-cumulus modification of these Pt-rich phases to cumulate processes, and particularly to interactions with trapped intercumulus liquid, as revealed by trace element zonation in cumulus orthopyroxene revealed in detail at thin-section scale in the Maia XFM images.

The critical advantage of fast XFM using the Maia detector is that it allowed for identification of sufficient numbers of grains to be able to draw statistically significant inferences about the detailed microtextural environment of the grain population. The XFM-based search technique has the capability of being able to locate all of the Pt-rich grains greater than about 0.5 μm in size in the entire sample volume, in contrast to selective polishing and SEM searching techniques which inevitably miss a large proportion of finer grains. Detailed follow-up using conventional SEM with and without focussed ion beam milling allowed identification of the specific phases where these occurred close to the sample surface.

Interaction of platinum-group elements with trapped intercumulus liquid is an issue at the heart of a long-running debate on the origin of PGE mineralization in layered intrusions. A series of papers (Ballhaus and Stumpfl 1986; Boudreau et al. 1986; Boudreau and Meurer 1999)

has attributed PGE mineralization to the transport of PGEs by evolved late magmatic fluids derived from advanced crystallization of intercumulus liquid, ascending through the cumulate pile during solidification. The combination of observations available from XFM, particularly the precise siting of PGE minerals in relation to subtle trace element zonation in cumulus silicates, allows the relationship between PGMs and trapped liquid solidification to be examined in a new way. Results have far-reaching implications for PGE geochemistry in general, and for the genesis of stratiform PGE mineralization in layered intrusions.

Methods

X-ray fluorescence microscopy (XFM)

X-ray fluorescence (XRF) microscopy was performed on the XFM beamline at the Australian Synchrotron in Melbourne (Paterson et al. 2011) using the Kirkpatrick Baez mirror microprobe end station. This provides a monochromatic 2-μm beam-spot size for energies in the range 4–20 keV. Equipped with the Maia 384 detector array, the XFM beamline can acquire data at 2 μm resolution from 384 detectors simultaneously over areas of several square centimeters (Kirkham et al. 2010; Ryan et al. 2010) with count rates of ~4–10 M/s at an energy resolution of 300–400 eV for the version on which these experiments were conducted; the current MaiaC array has an energy resolution of 240 eV. These spectra are then processed by the GeoPIXE software into element concentrations represented as maps. The X-ray beam penetrates the entire thickness of the sample such that the maps have 2 μm resolution in X and Y but are not directly resolvable in the Z direction, although Z direction depth can be inferred from data processing.

In this study, large-area 2 cm^2 element maps were collected on each of seven samples with an incident beam energy of 18.5 keV, a spot size of 2 μm, and dwell times per pixel of 0.97 ms to locate areas where Pt-rich inclusion were observed. For each area identified, follow-up maps of selected subareas were collected where Pt grains were tentatively identified. These additional maps were collected with dwell times of 15.26 ms per pixel to enhance the signal-to-noise ratio and improve quantification. At these scanning rates, the spatial resolution is approximately the same as the beam diameter.

The synchrotron data for each map were analyzed with the GeoPIXE software suite which uses a fundamental parameters approach, with spectral deconvolution and imaging using the dynamic analysis method and a detailed model of the Maia detector array efficiency (Ryan et al. 2010; Paterson et al. 2011). Data were fitted using a yield file which calculates the effects of X-ray absorption by the given matrix or mineral phase (Ryan et al. 2000). In this study, the Monts de Cristal pyroxenes were fitted assuming a 125-μm-thick pyroxene matrix backed by a 1 mm pure quartz glass slide. Depths to PGM aggregates were determined by comparing spectra from the inner and outer portions of the Maia detector array according to the method of Ryan et al. (2014a), and used to select grains close to the surface for further investigation by PIXE and SEM. The scans are carried out in air, resulting in attenuation of X-rays lighter than Ca Ka. This limits the range of detectable elements. Of those elements commonly associated with Pt, the technique can detect ~100 ppm levels of Ir, Os, Se, Bi, Sb, As, Pb, and Sn, but not the light PGEs (Rh, Ru, Pd) or S. (The revision C Maia detector array is capable of detecting S).

Proton-induced X-ray emission microprobe (PIXE)

Regions pinpointed to contain PGE inclusions by XFM analysis were selected for μ-PIXE analysis to both confirm synchrotron data and ascertain elemental quantities missed by XRF. Proton energy loss through a mineral is able to excite energy levels well beyond those of XRF and hence able to detect a higher portion of the periodic table including S, Te, Sb, and Rh. Particle-induced X-ray emission (PIXE) on the CSIRO nuclear microprobe (NMP) employed a 3-MeV proton beam focussed to around 2 × 4 μm in this instance. Regions were scanned and data collected using the MicrodaQ system of Laird et al. (2013) with beam currents typically in the 1–2nA range. Scan sizes ranged from 20 to 40 μm. Post-processing was carried out using the GeoPIXE software, using the same pyroxene yield curve and applying some of the concepts discussed above.

High-resolution X-ray computed tomography (HRXCT)

Three 2 × 2 mm chips were cut from selected areas (boxes 80152, 80155, and 80157, respectively) around Pt–As–Cu–Ni aggregates of the thin sections used for the XFM study. Each chip was scanned using a XRADIA XRM500 3D X-ray microscope installed at the Australian Resource Research Centre (CSIRO, Kensington, Western Australia) with X-ray source and detector positions optimized to have a voxel size of 0.9 μm and phase contrast. Data were processed using a slightly modified version of the method described in Godel (2013). Four Pt–As–Cu–Ni sulfide aggregates were imaged at high resolution in 3D. The depth of each aggregate within the sections was calculated by fitting a plane perpendicular to the thin-section surface with the plane also crosscutting the barycenter of each particle.

Results of the CT scans replicated within 10 % the depth of the grain below the surface of the sample as determined by analysis of the Maia spectra as described above.

Focussed ion beam milling and SEM

Grains calculated to be buried within 10 μm of the surface were excavated using a Tescan Lyra Dual Beam SEM equipped with a Ga focussed ion beam. Following excavation, the grains were imaged, and the distribution of chemical elements was mapped using energy-dispersive X-ray (EDX) spectroscopy. Mapping was carried out using an Oxford Instruments X-Maxn silicon drift X-ray detector and Oxford Instruments Aztec software. Low-energy electron beams (~7 keV) were used to reduce the X-ray generation volume of the beam, thereby increasing spatial resolution, while obtaining the range of X-ray energies necessary to discriminate between key elements. For As-bearing grains, higher energy maps were also made to verify the presence of As using the K-lines because the L-lines overlap with Mg that is present in the Opx matrix. Several grains were calculated to be at or within 1 μm of the surface, and these were imaged with no FIB excavation. An additional grain was found within sample PX21B using an automated bright-phase search on a Tescan Tima equipped with three Pulse Tor detectors.

Geological setting of the Monts de Cristal Complex

The Monts de Cristal Complex is a layered mafic–ultramafic intrusion in Gabon, containing layers of anomalously Pt-enriched pyroxenite, with one particularly enriched zone. The geological setting is described in detail by Maier et al. (2015), and only a brief summary is given here. The Monts de Cristal Complex, locally also referred to as the Kinguele Complex, is located in NW Gabon, some 70–150 km to the NE of Libreville, and ~50–100 km north of the Equator (Fig. 1). It consists of several igneous bodies interpreted to be remnants of a tectonically dismembered, >100 km long and 1–3 km wide, ultramafic–mafic intrusion (Edou-Minko et al. 2002; Maier et al. 2015). It is the most significant mafic–ultramafic layered complex yet identified on the Congo craton. The Complex consists largely of orthopyroxenite cumulates, with less abundant olivine–orthopyroxenites and norite, and rare harzburgites and dunites. Geochronology using U–Pb SHRIMP on baddeleyite indicates an age of 2775 ± 11 Ma and on monazite 2765 ± 11 Ma. The rocks have fractionated incompatible trace element patterns showing strong relative enrichment in LREE and LILE, and negative Nb–Ta and Ti anomalies. Initial Sr isotope ratios of plagioclase are 0.7024–0.7028 (εSr ~ +20), εNd of whole rocks is −0.6 to +0.3, and $\delta^{18}O$ of orthopyroxene is +7.38 to +10.45. These data indicate the presence of an enriched component, possibly derived from crustal contamination of a magma generated from a mantle plume. Mineral compositions (Fo_{ol} 84, $Mg\#_{opx}$ 85, An_{plag} 60–68, Cr/Fe chromite 1–1.45) and whole-rock data suggest that the magma was a low-Ti basalt containing approximately 10 % MgO and 0.5 % TiO_2. Most rocks show an unusual pattern of strong Pt enrichment (10–150 ppb) at low concentrations of Pd (1–15 ppb), Au (1–2 ppb), and Cu (1–20 ppm).

Pt-enriched pyroxenites

Pt-enriched orthopyroxenites within the complex contain 30–150 ppb Pt, up to 15 ppb Pd, 4 ppb Ir, 9 ppb Ru, 6 ppb Rh, and 3 ppb Au. The highest Pt values occur in a specific layer that can be correlated laterally for several 100 m, and Pt concentrations within the anomalous unit have a median value around 70 ppb. Platinum and Pd show no correlation, and there is no associated anomalism in either Ni or Cu. Platinum concentrations in the pyroxenite layer are very homogenous across the intrusion. The data cluster quite tightly from 20–120 ppb, with very few outliers. No economically significant magmatic sulfides have been detected within this unit, or elsewhere within the intrusion. Orthopyroxene has Mg# 78–85, 200–1000 ppm Ni, 0.4–0.7 % Cr_2O_3, and up to 2 % Al_2O_3 (Maier et al. 2015).

Results

Silicate petrography and pyroxene chemistry

The Pt-enriched samples studied were all orthopyroxenites, consisting of over 85 % euhedral bronzite grains in point or face contact, having typical grain sizes of 1–4 mm, with interstitial space occupied by cm-sized plagioclase oikocrysts and minor 2–4 mm interstitial clinopyroxene grains (Fig. 2).

Bronzite grains constitute a bimodal population (Figs. 2a, 3). The main mode comprises smaller inclusion-free euhedral to slightly rounded grains that lack internal zoning in Cr content (see below). The mode with larger grain size contains multiple inclusions of olivine and chromite and has subtle but distinct internal normal (i.e., Cr-rich cores, Cr-poor rims) or oscillatory zoning with respect to trace Cr content. In most cases, this zoning defines a euhedral core. In others, the zoning is complex and appears to define multiple accreted cores within individual grains (Fig. 3d, f) that hint at a possible origin as inverted pigeonite. Plagioclase is uniformly unzoned.

Zoning is also evident in Ti, which is commonly enriched by about 30 % of the core abundance within a zone around 100–200 μm wide around the margins of

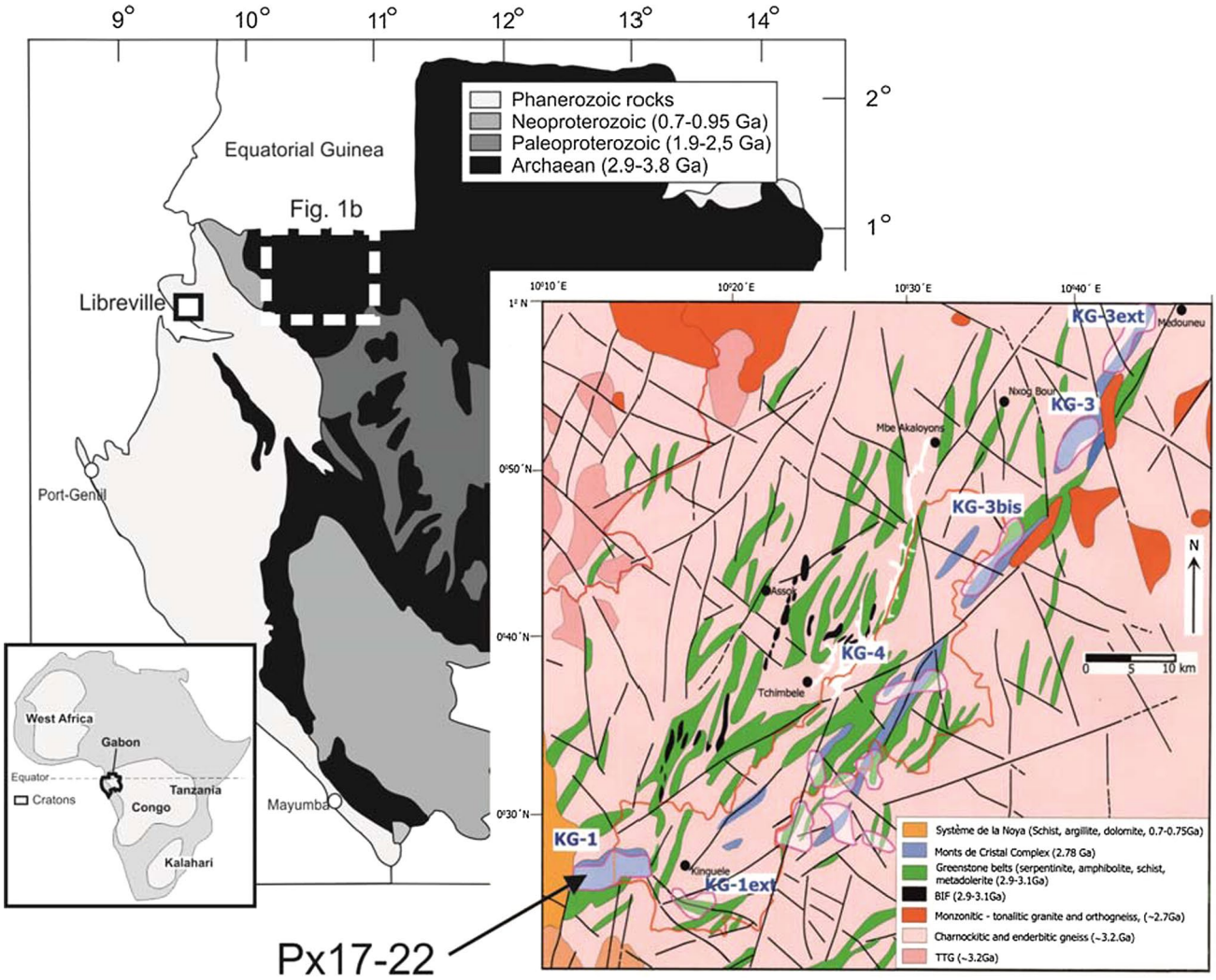

Fig. 1 Location map of the Monts de Cristal Complex, after Maier et al. (2015)

otherwise homogeneous bronzite grains. This marginal zonation is most evident in areas where multiple small bronzite grains are in contact with one another, and is absent where bronzites are enclosed within plagioclase oikocrysts.

Pt mineral associations and disposition from synchrotron XFM imaging

Over 100 individual Pt-rich grains were imaged on the XFM beamline of the Australian Synchrotron in six thin sections of 125 µm thickness. Of these grains, only three were observed exposed on the sample surface. This is expected given the very small grain sizes. As a consequence of this, and the unknown orientation of grain boundaries within the 125 µm thickness of the section, it is impossible to state definitively whether most of the imaged grains are located precisely on grain boundaries, except where those gains have also been located in micro-CT scans or FIB-SEM images, and also the extent to which they are precisely colocated in 3D with the other associated elements. However, the relatively large number of observations allows us to make some robust statements about element locations and associations. Locations of Pt-rich grain occurrences in relation to pyroxene grains are shown in Fig. 4 for one typical sample out of the six samples investigated.

All occurrences of Pt grains identified in preliminary scans of approximately 2 × 1–4 cm areas were followed up by detailed scans over Pt hot spots over areas around 100–200 × 200–400 µm (small numbered boxes in Fig. 4), using longer dwell times. Representative examples of the multi-element images obtained over these detailed boxes are shown in the supplementary material. Detailed examples showing three distinct types of Pt–As–sulfide

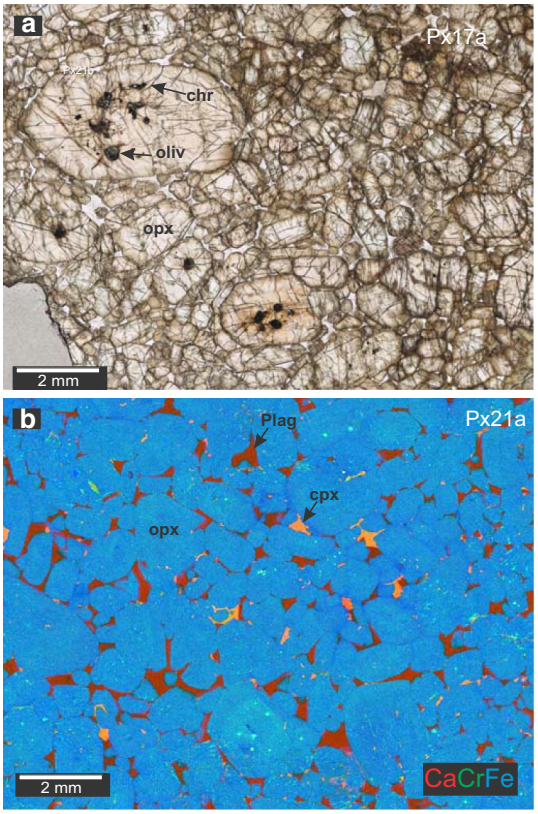

Fig. 2 Photomicrographs of Monts de Cristal Pt-enriched pyroxenites. **a** Plane-polarized transmitted light micrograph of sample Px17a, approximately 125-μm-thick section. **b** XFM three-element false-color map, showing Ca (*red*), Cr (*green*), and Fe (*blue*), normalized to range of variability for each element, linear scale for Sr and Fe, logarithmic scale for Cr. *Blue areas* are orthopyroxene (Cr enriched in lighter areas), *orange* clinopyroxene and red plagioclase

association, including one example of an association with enclosed chromite, are shown in each of the confirmed Pt grain associations has been classified according to two criteria:

1. *Elemental associations*; specifically, whether Pt-rich grains occur within a few tens of μm of other phases containing Ni or Cu, or with As-rich phases. In a few cases, all of these elements are directly associated on a micron scale. Sulfur is undetectable on this version of the Maia detector array, but the speciation of Ni and Cu as sulfide minerals is confirmed by petrographic observation; sulfide phases are pentlandite and chalcopyrite with minor bornite. Detectable Se was noted in common association with "buried" Ni–Cu phases, serving as a reliable proxy for S and supporting the presence of Ni and Cu as sulfide grains. In two of the sections studied, depth-to-grain estimates were made for both Pt and As by comparing peak intensities in the inside and outside elements of the Maia detector array (Ryan et al. 2014a), and in all cases where both elements were observed to be coincidental in the 2D image, they were also found to be at the same depth within approximately 10 % of the depth. Hence, where Pt and As are colocated they can confidently be assumed to be within the same phase.
2. *Spatial association with silicate mineral microenvironment*. A number of different settings were observed (Fig. 4), of which the most common were at (or within <100 μm of) orthopyroxene–plagioclase contacts, where the opx shows no trace element zoning, and at grain boundaries between adjacent opx grains, typically but not always showing minor marginal zonation in Ti.

Both element and spatial associations are tabulated in Table 1, and spatial associations are summarized in Fig. 5. The main results are summarized as follows, for the 80 grains where observations were considered reliable. Taking all grains together, 64 % are spatially coincident with an As spike, implying the presence of Pt in an As-bearing phase; 84 % are either closely spatially associated or coincident with Se-, Cu-, and/or Ni-rich phases and of these 49 % are precisely coincident in 2D with Cu- and/or Ni-rich phases. Spatially, most grains (72 %) are located at opx grain boundaries not in contact with plagioclase, and 28 % at opx-plag boundaries with or without other phases. Of these groups, there is no significant difference in the element associations. Considering grains at opx–plagioclase boundaries and opx–opx boundaries, 62 and 63 %, respectively, are arsenide phases, 52 and 43 % are coincident with sulfide phases, and 90 and 80 % are either coincident with or proximal to sulfide phases. This indicates that there is no systematic variation in either mineralogy or sulfide association depending on whether or not grains are located within plagioclase oikocrysts, or within zoned rims of opx grains outside oikocrysts.

Of all the grains observed, no more than 5 % are located within the population of large, Cr-zoned inclusion-bearing opx grains (e.g., Fig. 6c); however, these grains are relatively rare so the proportion may simply reflect the baseline abundance and is not regarded as significantly different from the overall population.

The XFM data allow for semiquantitative determination of element concentrations over sampled volumes within specified areas of the section; examples of specifically selected areas for analysis are shown as the green outlines in Fig. 6. Approximately 60 such volumes were measured over four different sections, and results are plotted in Fig. 7, subdivided by elemental association, with each point representing the analysis over the entire outlined volume.

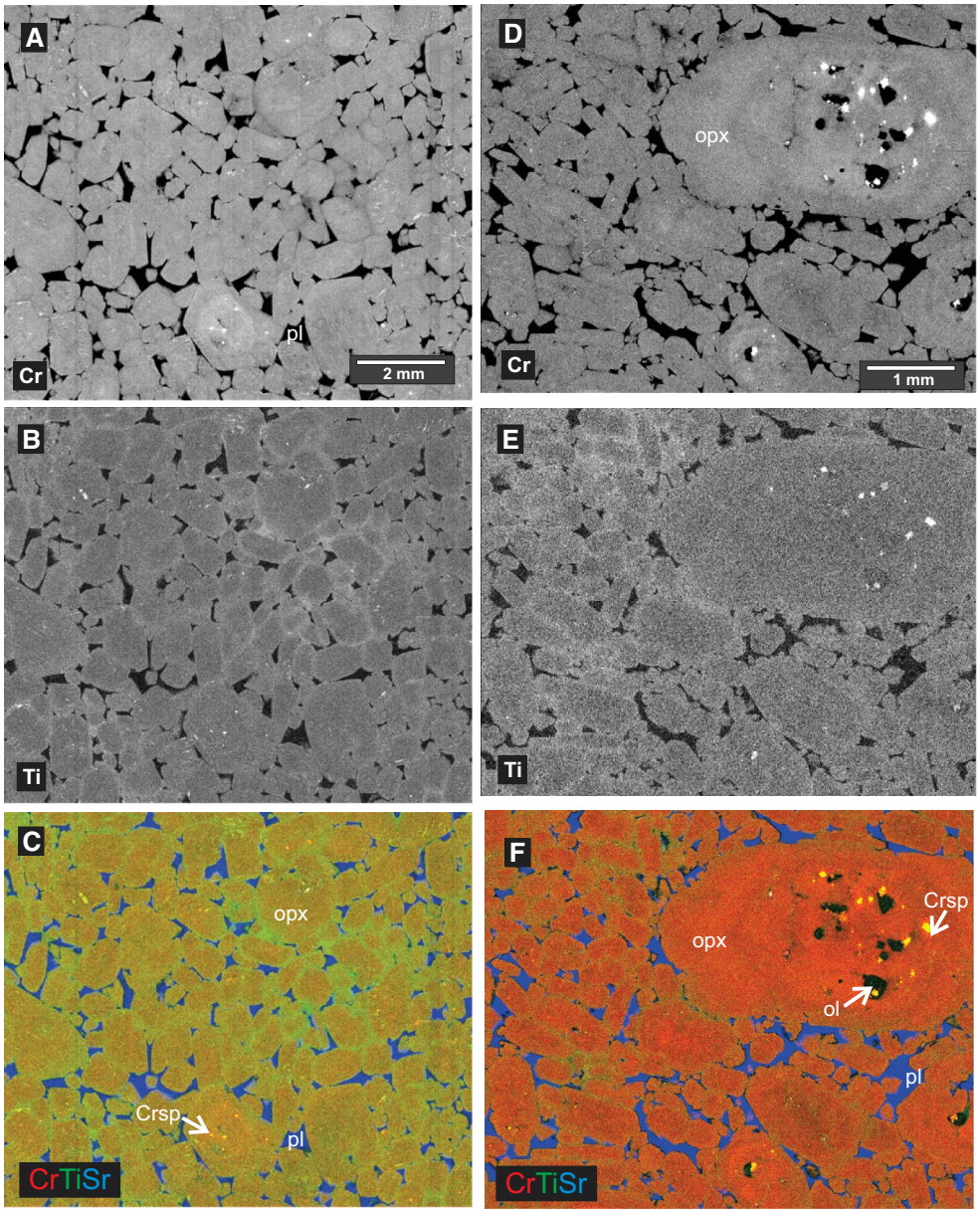

Fig. 3 XFM element maps showing trace element zoning in orthopyroxenes. Images **a–c** from sample Px21a, **d–f** from Px17a. **a**, **b**, **d**, **e** are single-element *grayscale* images based on background corrected count rate on Ka peak, linear for Ti and log-transformed for Cr. Minimum and maximum values for Ti and Cr in orthopyroxene are about 700 and 1000 ppm, respectively, for Ti and 2100 and 2700 ppm for Cr, based on quantitative standardless determinations from GeoPIXE software reduction in the Maia XFM spectral data. **c**, **f** three-element RGB maps, Cr (*red*)–Ti(*green*)–Sr(*blue*) showing heteradcumulate texture of plagioclase oikocrysts (*blue*, due to high Sr and low Cr, Ti) interstitial to opx with minor intercumulus cpx (*red–orange* to *green*). Each element is scaled to maximum values. *Light green* highlights on both images are small chromite inclusions, preferentially located in grains showing Cr zoning. Note subtle complex internal zoning in Cr in some opx grains and fine rims of elevated Ti at opx–opx grain contacts lying outside the plagioclase oikocrysts, but not at opx–plag contacts

Where Pt hot spots are closely associated with Cu–Ni-rich phases, there is characteristically no correlation between any of the four elements Pt, Cu, Ni, and As apart from a weak association between high Cu and high Ni (Fig. 7) which corresponds to the larger sulfide aggregates such as that in Fig. 6c. These high Ni and Cu regions all have undetectable As. In one particular section, Px21, about two-thirds of the Pt hot spots show close association with As and have Pt/As corresponding closely to stoichiometric sperrylite ($Pt–As_2$) (Fig. 7c). In all of these hot spots, Cu and Ni contents are

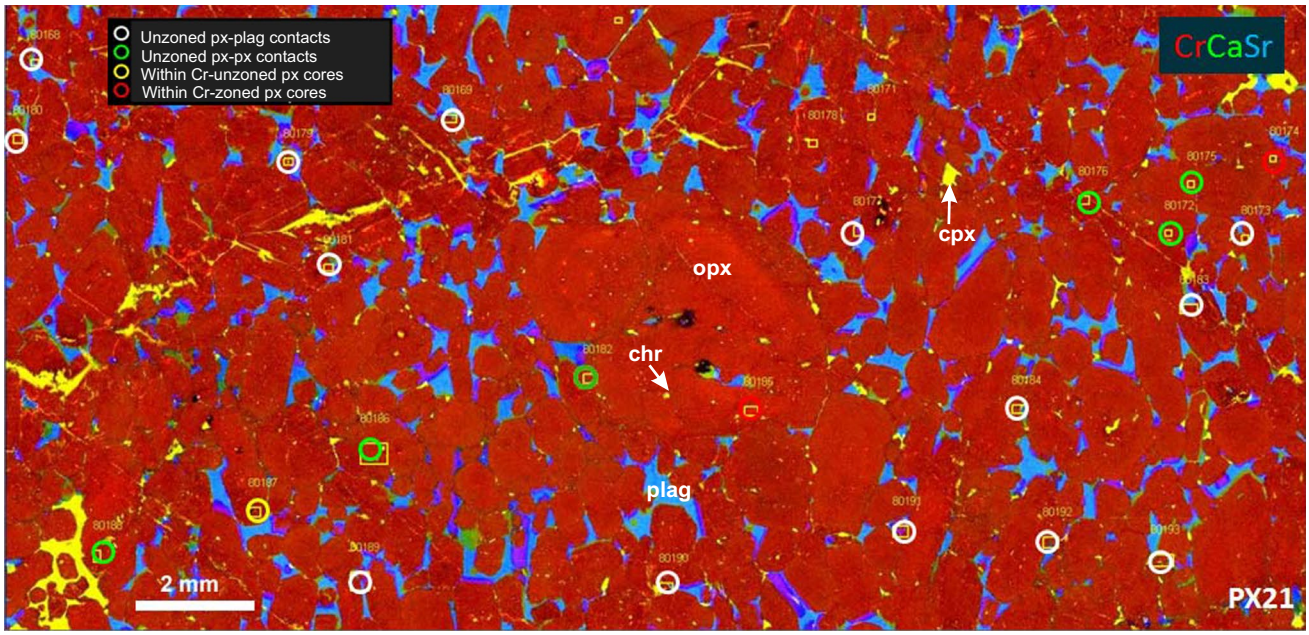

Fig. 4 False-color XFM map of an area of thin-section Px21 showing location of Pt grains in relation to silicate microenvironment. Cr (*red*)–Ca(*green*)–Sr(*blue*) map shows heteradcumulate texture of plagioclase oikocrysts (*blue*) interstitial to opx with minor intercumulus cpx (*yellow* to *green*). Each element is scaled to maximum values, Cr values log-transformed. Pt grain locations lie within *rings*, *color-coded* according to microenvironment. *Yellow boxes* indicate areas of detailed high-definition scans

very low implying a near-absence of sulfide. In the other three samples analyzed in detail, two (Px22, Px18) had 3 % of Pt-rich grains close to sperrylite stoichiometry and the remainder with much higher proportions of Pt to As; the 97 % are interpreted as mixtures of Pt arsenide and Pt–Fe alloys. This implies that Pt is present in the pyroxenite layer primarily as Pt–Fe alloys, with a minor heterogeneously distributed component of sperrylite, concentrated in particular subvolumes at approximately cubic centimeter scale.

These measurements allow an order of magnitude estimate of the relative proportions of Pt to Cu, taken as a proxy for sulfide abundance, and of Pt to As. Excluding the sperrylite-dominated sample Px21, we obtain median values of Pt/Cu and Pt/As of 1.3 and 50, respectively. Fifty percent of Pt/Cu values (between first and third quartiles) fall between .05 and 9, and 80 % (between first and ninth deciles) between .001 and 13. For Pt/As, the corresponding figures are 7 and 120 for first and third quartiles.

MicroCT results

Three 2 × 2 mm chips were cut from selected areas (boxes 80152, 80155, and 80157, respectively) around Pt–As–Cu–Ni aggregates of the thin sections used for the XFM study. Four Pt–As–Cu–Ni sulfide aggregates were imaged at high resolution in 3D. The depth or each aggregate within the sections was calculated by fitting a plane perpendicular to the thin-section surface with the plane also crosscutting the barycenter of each particle. Depth estimates agreed within 10 % with those determined from the XFM data, corroborating the validity of this depth estimation method. The grains imaged all fall precisely on pyroxene grain boundaries.

PIXE results

PIXE analyses (proton-induced X-ray excitation) on the nuclear microprobe (NMP) at the University of Melbourne were used to test and reproduce the synchrotron observations and to potentially detect a wider range of elements (particularly light elements, and soft L-line X-rays such as Pd, Ru, and Rh). The method was applied to a subset of Pt hot spots that were determined to lie within the top 20 μm of the section on the basis of the GeoPIXE depth-to-grain calculation.

Results from PIXE (Fig. 8) generally confirmed the element associations obtained using synchrotron XFM, and for the most part, no additional non-PGE elements were detected. This is in part owing to the target grains being buried, such that S was not detectable by either method, but the PIXE method would be expected to detect other PGEs, Bi and Te if present in appreciable quantities in any of the imaged phases. The only other PGEs detected were Rh, which appeared coincident with Pt and As in three of the four detailed scans, and is probably present in the imaged phase at major element concentrations, and Ru, which appeared coincident with Pt in one scan.

Table 1 Catalogue of Pt grains encountered in Maia XFM mapping. Numbers of grains in intersecting spatial occurrence category (mineralogy of enclosing phases), and sulfide–arsenide association

Occurrence at contact of	Pt–As–Ni–Cu association—count of occurrences										Total	Percentages		
	No As, no S	No As, prox S	As No, S Col	As prox, S no	As prox, S prox	As prox, S col	As Col, S No	As Col, S Prox	As Col, S Col	Other		Arsenide phase colocated (%)	Sulfide colocated (%)	Sulf proximal or colocated (%)
OPX boundary	2	3	1	1	4	5	6	11	6		39	59.0	30.8	76.9
OPX internal							2	2	1		5	100.0	20.0	60.0
OPX–OPX–sulfide						4			4		8	50.0	100.0	100.0
OPX–OL–SUL									2		2	100.0	100.0	100.0
OPX–plag	1	3	2		1		1	4	8		20	65.0	50.0	90.0
OPX–Plag–Sulfide						1					1	0.0	100.0	100.0
(blank)						1			4		5	80.0	100.0	100.0
Total	3	6	3	1	5	11	9	17	25	1	80	63.8	48.8	83.8
Opx–plag combined	1	3	2	0	1	1	1	4	8	0	21	61.9	52.4	90.5
Opx no plag	2	3	1	1	4	9	8	13	13	0	54	63.0	42.6	79.6

No As No S = no proximity to As- or Cu–Ni sulfide phase; As Prox, S Prox = within 50 microns of As- or Cu–Ni sulfide phase

As Col, S Col = colocated (implying in same phase with) As, and/or Cu and/or Ni. As Col, S No = As-bearing phase, no association with sulfide

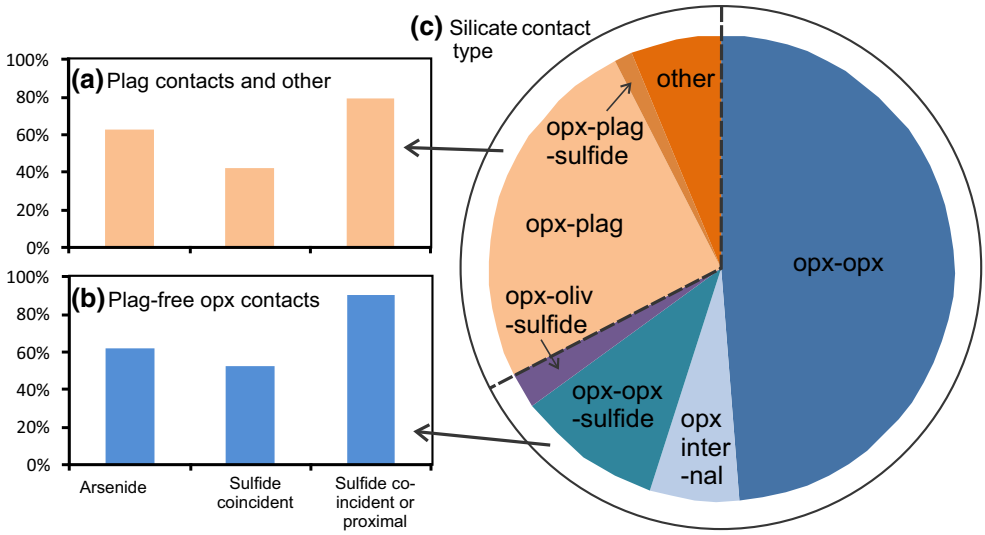

Fig. 5 Charts showing spatial associations. **a**, **b** proportion of Pt-rich grains occurring as As-bearing phases, coincident with Ni and or/Cu sulfide, and either coincident with or within 50 μm of Cu–Ni sulfide phases, for grains occurring at contacts of plagioclase oikocrysts with opx (**a**) or at plagioclase-free opx contacts outside oikocrysts (**b**). **c** proportions of all Pt grains (80 observations) occurring in various textural relationships to silicate phases. *Blue* and *pink/orange shades* correspond to categories in (**a**, **b**)

FIB-SEM observations

Focussing on Pt-rich grains identified as lying close to the sample surface by analysis of the synchrotron XFM data, we were able to contain direct images of the various detailed types of Pt mineral occurrence. These include euhedral Pt alloy and sperrylite grains with no associated sulfide grains lying just inside orthopyroxene grain rims (Fig. 9a, b), Pt alloy grains lying inside Cu-rich sulfide "microblebs" associated with late-stage fractionated intercumulus melt pockets (Fig. 9c), and composite grains of sperrylite with Cu-bearing phases (Fig. 9d, e) including one example of native Cu (Fig. 9h). One grain was found in association with an unidentified Ag-rich phase (Fig. 9j). Numerous examples were observed of sulfide grain aggregates associated with late-stage intercumulus pockets enriched in highly incompatible components such as Th and Zr (Fig. 9c); this example has a Pt grain enclosed within sulfide, but most such occurrences are not associated with Pt-rich phases. Numerous few-micron-wide cavities, interpreted as fluid inclusions, were observed along silicate grain boundaries, but without any specific association with Pt phases.

Discussion

Critical observations

Platinum occurs as discrete grains of Pt minerals with no detectable Pd, Os, or Ir and only minor Rh and Ru. These minerals are predominantly alloys, arsenides and/or sulfarsenides, with no detectable Bi or Te and minor Se. A small proportion of these phases can be identified as sperrylite, while most others are likely to be Pt/Fe alloy, as confirmed by selective SEM imaging.

The majority of grains occur in spatial association with Cu- and/or Ni-bearing sulfide grains, although in most cases the Pt grains themselves are not sulfide minerals. In about half of the occurrences observed, the Pt phases are not in physical contact with base metal sulfide minerals, and in one particular sample, Pt is carried primarily as sperrylite with no spatial association to sulfides. The relative abundances and volumes of Pt minerals to sulfide minerals is very large compared with typical magmatic sulfides. Estimates of the relative proportions of Pt to Cu within the Pt "hot spots" as shown in Fig. 6, taken as a proxy for sulfide abundance, fall between about 0.1 and 10 with a median around 1 in these samples. These values are greatly outside the range of typical magmatic sulfide liquids: Pt/Cu ranges from around .00001 in Ni–Cu-dominant ores to 0.01 in highly Pt-enriched reef-style sulfides, the only exception being some of the extreme values of around 0.01 to 0.1 for Pt/Cu estimated for bornite–skaergaardite aggregates in the Platinova Reef of the Skaergaard intrusion (Godel et al. 2014).

Platinum minerals occur predominantly at the margins of cumulus opx grains and show no systematic difference in mineralogy, sulfide association, or arsenide association depending on whether the host grain boundaries fall inside or outside plagioclase oikocrysts. The implications of this observation are considered next.

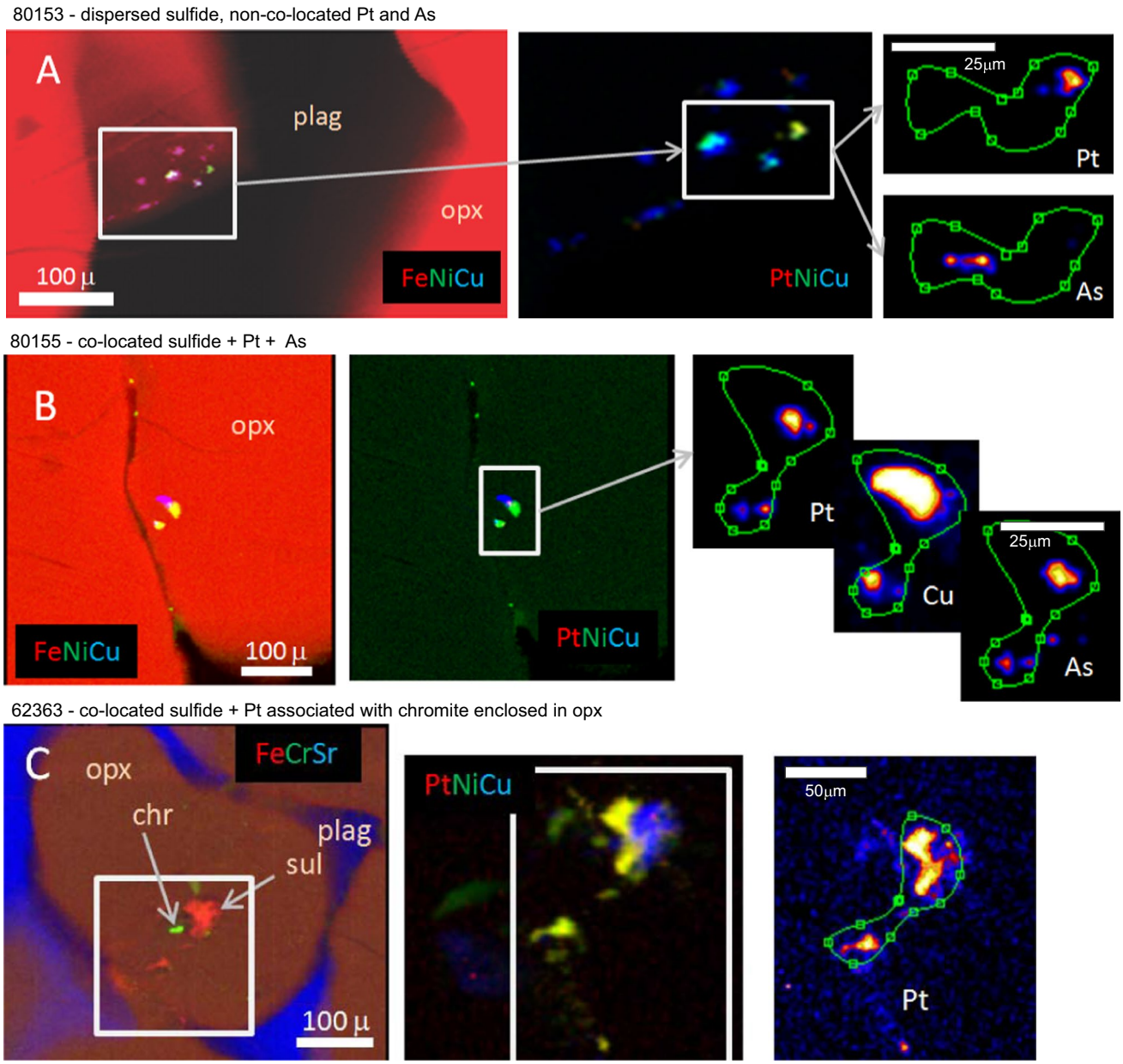

Fig. 6 Sets of three-element maps for examples of three distinct types of Pt–As–sulfide association. **a** Discrete non-coincident Pt, As, and Ni–Cu hot spots on a pyroxene grain boundary in contact with plagioclase, sample Px18. **b** Coincident Pt, As, and Cu on an opx–opx grain boundary, sample Px18. C, rare example of a coincident Pt, Ni, and Cu association with no detectable As associated with a chromite inclusion inside an opx grain, sample Px17b. *Green outlines* indicate the area over which quantitative Pt, As, and Cu values were integrated to generate the inter-element correlations illustrated in Fig. 7

Relationship of Pt associations with the presence of plagioclase oikocrysts

The origin of poikilitic textures has been the subject of long-running debate, with interpretations running from growth from the trapped intercumulus liquid within a segregated crystal mush (Wager et al. 1960; Wager and Brown 1968) to origin as essentially cumulus phases, forming by in situ growth in a crystal mush boundary layer between the cumulus crystal pile and the adjacent body of flowing or convecting magma (Campbell 1968; McBirney and Noyes 1979; Mathison 1987; Godel et al. 2013). Regardless of the favored model, highly efficient expulsion of residual trapped liquid is required to account for the incompatible-depleted and trapped-liquid-free character of heteradcumulate such as those sampled here. It is clear from observations on the Monts de Cristal pyroxenites that the plagioclase oikocrysts formed very early in the

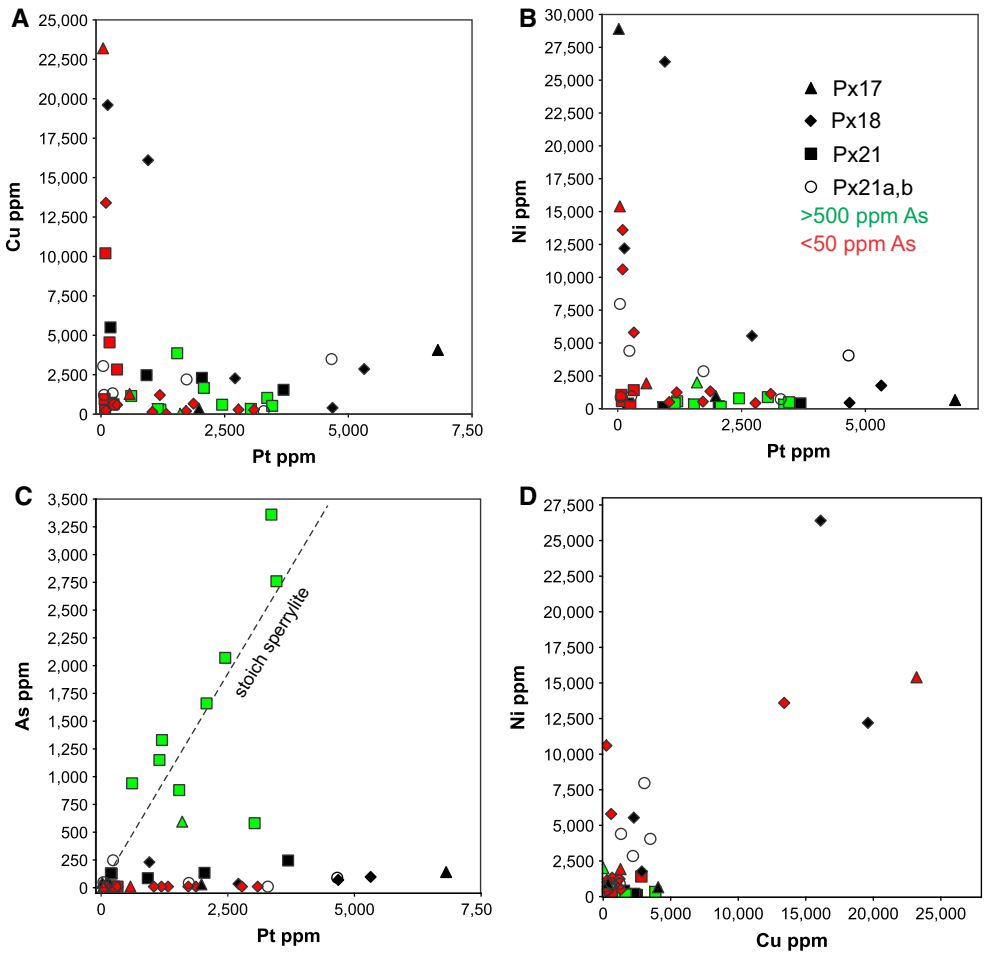

Fig. 7 Analyses of Cu, Ni, Pt, and As over subvolumes of detailed scans, such as those indicated by *green outlines* in Fig. 6

crystallization history, either simultaneously with or immediately after the accumulation (by whatever means) of the cumulus pyroxene grains. This is necessary to account for the absence of Ti-enriched rims, presumed to have formed by reaction with migrating trapped liquid, in grains trapped within the plagioclase oikocrysts. The microdomains of Ti rim enrichment are the remains of expulsion pathways of reactive, fractionated trapped liquid migrating out the cumulus mush layer through pore space between the oikocrysts.

Relationship of Pt phases to oikocrysts and trapped liquid reaction

The key observation in this context is that the mineralogy and composition of the Pt–As–Cu–Ni association is completely unaffected by this trapped liquid migration process. There is no difference in mineralogy or element ratios between Pt-rich associations inside or outside the oikocrysts, i.e., between those shielded from trapped liquid migration by early bottling in oikocrysts, and those exposed to the Ti-enriched migrating trapped liquid (Fig. 5). This is a significant observation: models for formation of PGE Reefs by upward migration of fractionated residual fluids or highly evolved expelled magma would predict that unprotected grain boundary locations outside oikocrysts should show evidence of this late fluid interaction. Either they should be deposition sites, in which case there should be a preferential association with Ti-enriched rims, or they should be dissolution sites, in which case these boundaries should be deficient in Pt phases, and depleted in Pt relative to sulfide components. The data presented here imply that the Pt phases formed early, as cumulus phases, and were not deposited from migrating intercumulus fluids.

Relationship to cumulus sulfides

Platinum phases located in this study show a strong tendency to be colocated with very small volumes of base metal (Cu, Ni) sulfides, and sulfides are widely distributed in very small concentrations through all of the samples studied. In some cases, as noted above, the Pt-rich phases

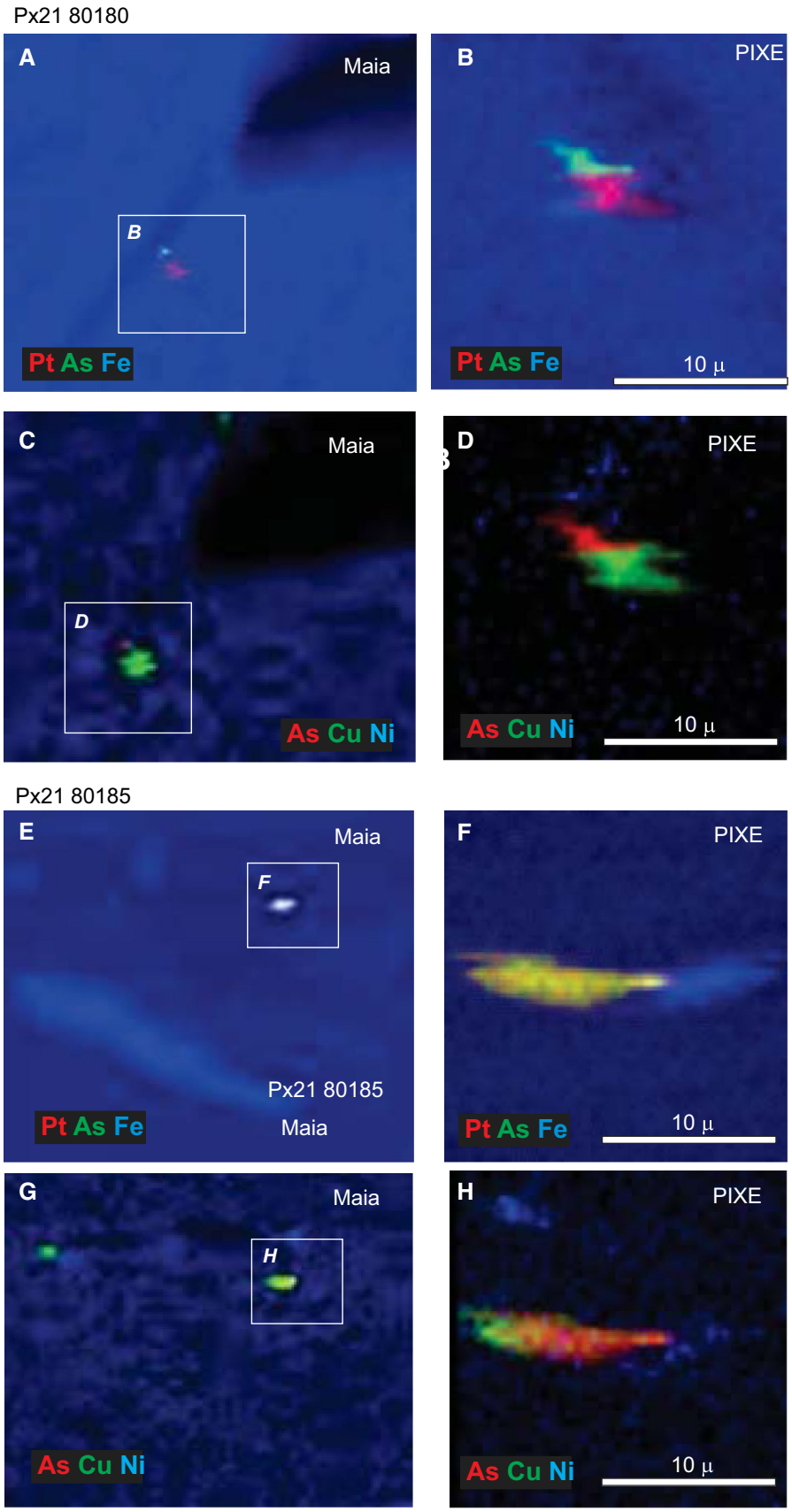

Fig. 8 Comparison of PIXE with XFM results—three-element false-color maps for Pt–As–Fe (**a**, **b**, **e**, **f**) and As–Cu–Ni (**c**, **d**, **g**, **h**) from XFM (*left*) and PIXE (*right*) for two Pt hot spots close to the sample surface in sample Px21

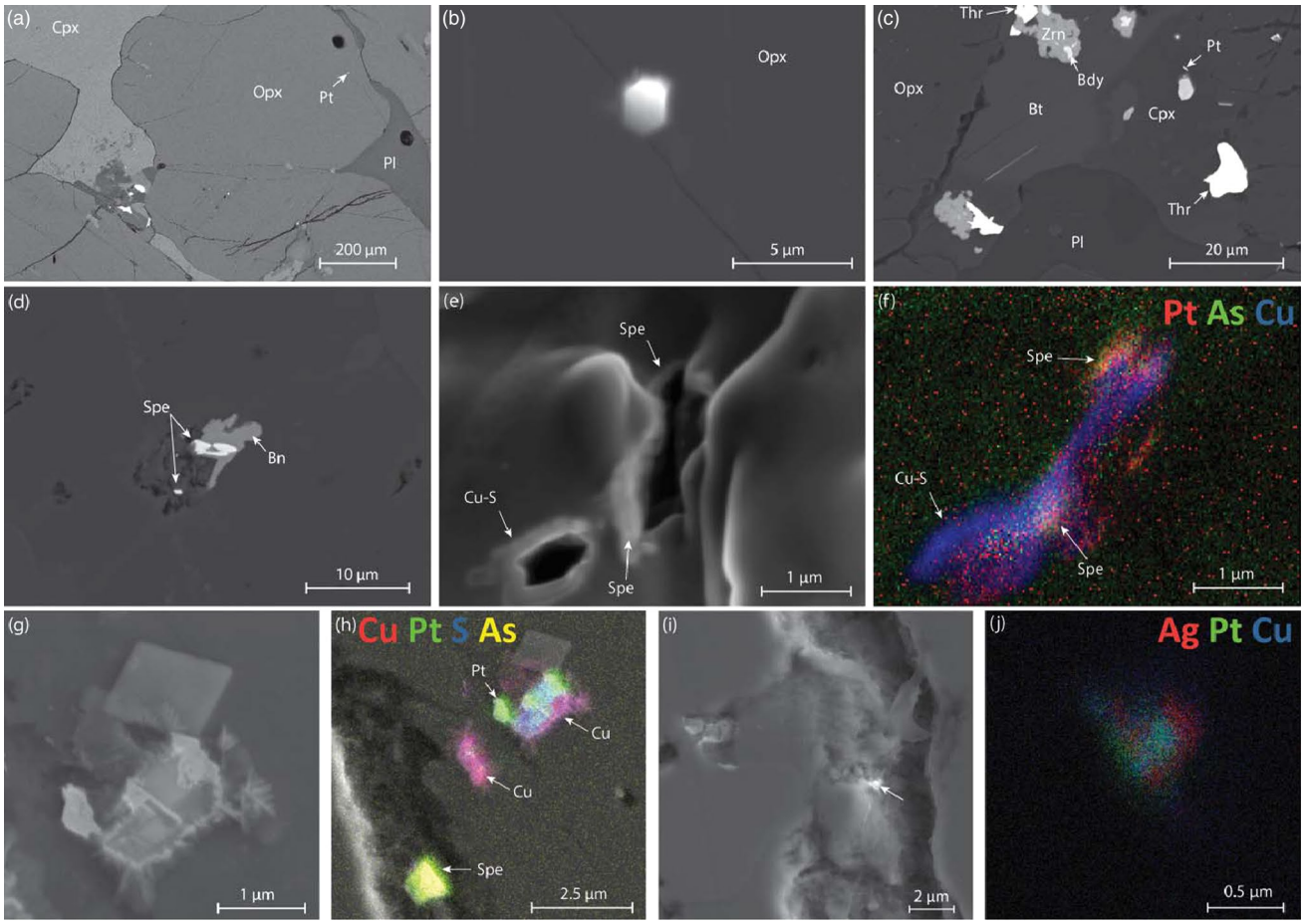

Fig. 9 SEM micrographs of Pt-bearing phases. **a** BSE image from showing a Pt grain located along an Opx grain boundary (**b**) in PX18 box 62364. **b** Close-up of euhedral Pt grain from (**a**) containing 2–3 wt% Rh. **c** Pt located within a late hydrous melt pocket. Sulfide grain beneath Pt grain also contains a semiburied Pt grain. **d** Sperrylite (Spe) and bornite in sample PX21B. **e** Sperrylite and Cu–S excavated using a focussed ion beam (FIB) from ~5 µm beneath the surface of sample PX21 box 80171. Inclusions appear to be hollow. **f** EDX chemical map of Pt (*red*), As (*green*), and Cu (*blue*) distribution within the FIB pit. Cu occurs with sulfur (not shown), and As occurs with Pt as sperrylite. **g** Secondary electron image (7 keV) of a Pt grains at the surface in sample PX21 box 80180. The spatial distribution of elements is shown in the EDX map in (**h**). Cu dendrites are growing from the edge of the Pt and S grain adjacent to a euhedral chromite. **h** EDX map (7 keV) showing Cu (*red*), Pt (*green*), S (*blue*), and As (*yellow*) distribution. **i** SE image (10 keV) of a Pt-bearing grain, indicated by a *white arrow*, at the surface within sample PX21 box 80173 along a boundary in Opx. **j** EDX map showing spatial variations in Ag (*red*), Pt (*green*), and Cu (*blue*). No As or S was present in this grain

can be identified as sperrylite, but in most cases it is an unresolvable mixture of Pt arsenide, some non-As, non-Se-bearing phase most likely to be a Pt–Fe alloy, associated in about two-thirds of cases with highly variable but generally low proportions of Ni-rich and Cu-rich sulfide but not usually in direct contact with that sulfide. This raises the question of whether sulfide liquid played a critical role in the nucleation and precipitation of magmatic Pt minerals. There are two possibilities.

Firstly, Pt and As may have been scavenged by tiny droplets of cumulus magmatic sulfide liquid, accumulating with the pyroxenes. The observation that the Pt phases are in close association but commonly not in direct contact with the sulfide phases, and also that the proportion of Pt to S and Pt to Cu is orders of magnitude higher than in typical magmatic sulfides implies that some subsequent dissolution or resorption of sulfide liquid into the silicate melt occurred at some point prior to the entrapment in plagioclase oikocrysts; this requires a very narrow window of timing giving the demonstrably early origin of the oikocrysts. Two possible mechanisms exist: dissolution of sulfide liquid following incorporation into sulfide-undersaturated magma, or preferential oxidation of the FeS component giving rise to a smaller volume of residual PGE and Cu-enriched sulfide (Wohlgemuth-Ueberwasser et al. 2013). The major problem with either hypothesis is that Pt is overwhelmingly dominant over the other highly chalcophile PGEs; Pt/Pd values and Pt/Cu values in particular are much higher

than in any known conventional magmatic sulfide (Barnes and Lightfoot 2005). The inferred As content is also very much higher. There is no plausible mechanism by which incongruent dissolution of originally "normal" magmatic sulfide would selectively remove Pd but not Pt. Furthermore, Maier et al. (2015) present a number of lines of geochemical evidence against the presence of a cumulus magmatic sulfide component in the Pt-enriched pyroxenites. They show that there is a strong positive correlation between whole-rock Ti, S, and Cu, indicating that S and Cu are behaving as incompatible elements (i.e., contained entirely within the trapped intercumulus silicate liquid, and controlled by the trapped liquid abundance) and is not controlled by the independent abundance of a cumulus sulfide liquid phase. The ratios Cu/Pd and Cu/Zr, indicative of the extraction or accumulation of sulfide liquid, are within typical mantle values within the Pt-enriched pyroxenites.

This leads to a second hypothesis, which is that the primary phase to separate from the magma was an immiscible Pt–As–S–Ni–Cu liquid, present in sufficiently small proportions to not disturb the whole-rock geochemical parameters noted above; the magma became saturated in this unusual liquid owing to exceeding the solubility product of these components. We suggest an analogy with another occurrence of tiny abundances of extremely PGE-enriched sulfide with an outlandish composition: the Pd–Cu-rich sulfides of the Platinova Reef of the Skaergaard intrusion (Bird et al. 1991; Andersen et al. 1998; Karup-Moller et al. 2008; Godel et al. 2014; Nielsen et al. 2015). In the Platinova case, Godel et al. (2014) suggest that the magma essentially became saturated in Cu-Pd sulfide at a critical point in its differentiation history, but in the Skaergaard case the magma was As poor and already depleted in Pt at the time of reef formation (Holwell and Keays 2014). In the Monts de Cristal case, the magma may have been much less differentiated and attained saturation in a Pt–As-rich sulfide component first.

A number of authors have drawn attention to the presence of As-rich phases and possible immiscible sulfarsenide melts within natural and experimental magmatic sulfides, e.g., (Hanley 2007; Tomkins 2010; Godel et al. 2012; Prichard et al. 2013; Pina et al. 2015). Such a sulfide–arsenide component would be expected to be molten at the silicate liquidus. There is a wide field of immiscibility between sulfide and arsenide melts, and As-rich sulfide liquids would be expected to split into conjugate S-rich and As-rich components at As contents as low as 2 wt% (Helmy et al. 2013). Helmy et al. (2013) determined the solubility of Pt in As-saturated sulfide melts at 0.3–2 wt% and showed that Pt would partition strongly into either the As-rich melt above about 1150 °C, or into sperrylite below this temperature. The same experiments also indicate that Pd should partition equally strongly into the As-rich melt over the entire sulfide–arsenide melting range. Hence, if the assemblages we observe are the product of a magmatic arsenide melt, they should be strongly enriched in Pd as well as Pt. On this basis, it is unlikely that they are the product of collection by magmatic sulfide–arsenide liquids.

A third possibility is that the Monts de Cristal magma precipitated Pt metal and arsenides as solid cumulus phases under sulfide-undersaturated conditions, and these phases then reacted at the post-cumulus stage with magma or a late intergranular fluid phase to form the associated sulfide minerals. Experimental work by Canali and Brenan (2014; Canali and Brenan 2015) addressed the effect of As on Pt solubility in molten basalt. They found that Pt–As complexes in the silicate should add only an insignificant amount to the solubility of Pt metal. At fO_2 of NNO, basaltic liquid is cosaturated with Pt metal + Pt–As melt when the basalt contains 77–90 ppb Pt and 417–438 ppm As. Given the strong positive correlation of Pt solubility with fO_2, these results imply that Pt–As assemblages could have been on the liquidus of the Monts de Cristal magma at typical magmatic fO_2 somewhat more reduced than NNO. If the fO_2 were close to IW, then these phases might saturate at Pt and As concentrations of as little as 10 ppb and 10 ppm, respectively, which is anomalously high for As but not at all unusual for Pt. Hence, the conditions required for the natural assemblages might be a combination of high As due to contamination and low fO_2, both of could arise if the magma digested reducing As-rich sediments. However, evidence for unusually reduced conditions is lacking, and V contents in orthopyroxene are lower than would be expected under oxygen fugacities much below QFM.

An important observation was made at the stage of direct imaging of Pt phases by SEM: the relatively common presence of late-stage intercumulus sulfide grains, relatively low in Cu, without any associated Pt-rich phase. This trace but relatively common association indicates that much of the sulfide in the sample is derived by solidification of residual trapped liquid rather than forming at the cumulus stage. This tends to support the argument that the observed association of Pt phases with small sulfide grains is a result of interactions with final-stage solidification of late-stage grain boundary magmatic fluids carrying S.

In conclusion, we reject the hypothesis that the Pt concentration is due to a conventional magmatic sulfide component, and we favor precipitation of solid $Pt–As_2$, Pt–Fe alloy, and possibly other solid Pt-rich phases, followed by localized reaction with S-bearing silicate melt to generate the observed associated sulfide component. The alternative hypothesis is accumulation of an unusual Pt–As–Cu–Ni–S-enriched melt, but neither hypothesis is fully consistent with our current state of knowledge about solution properties of Pt and As in silicate melts. At present, we

lack enough detailed knowledge of the microkinetics of nucleation of Pt-rich phases from silicate or sulfide melts to be to decide definitively between the various hypotheses advanced here, but the observations are strong evidence for direct precipitation of primary Pt-rich phases at the cumulus stage.

Conclusions

A large number of Pt-rich "hot spots" have been imaged in the Pt-rich pyroxenite layer of the Monts de Cristal Complex using X-ray fluorescence microscopy (XFM), enabling the detection of buried phases at depths of up to one hundred μm within thick sections. Phase identification has been validated using PIXE and FIB-SEM imaging on selected grains. Combining these results with subtle trace element variations in pyroxenite grains measured by the XFM technique, we have demonstrated that the Pt-rich component formed as a cumulus phase or phases. While there is some evidence for incongruent dissolution of sulfide, there is no evidence that Pt was significantly mobilized by post-cumulus processes. This allows us to eliminate migration of intercumulus fluids as a precipitation mechanism, and also allows a confident inference that a Pt-rich component, containing very low levels of other PGE, precipitated directly from the magma as a cumulus phase or phases. A strong association with As and minor Cu–Ni sulfides suggests that the concentrating phase may have been a highly unusual, extremely Pt-rich sulfide liquid with very low contents of other PGEs, but the very high ratio of Pt to other PGEs and Cu precludes an origin by desulfidation of a normal magmatic sulfide liquid. We favor a mechanism of direct precipitation of solid sperrylite and Pt–Fe alloy followed by early post-cumulus sulfidation. These observations reinforce a growing body of evidence that fractionation of Pt from other PGEs in some magmatic systems is a consequence of a solubility limit for Pt and provides the first evidence that the saturating phase also contains As.

Acknowledgments This research was carried out on the X-ray fluorescence microscopy beam line at the Australian Synchrotron, Clayton, Victoria, Australia. We acknowledge financial support for this facility from the Science and Industry Edowment Fund (SIEF). We thank Martin de Jonge for his programming of complex scan control scripts and Kathryn Spiers for beamline assistance during the experiment. James Mungall provided helpful reviews of a preliminary draft. This work was supported by the Multi-modal Australian ScienceS Imaging and Visualisation Environment (MASSIVE) (www.massive.org.au). We acknowledge the support of the National Resource Sciences Precinct through the Advanced Resource Characterisation Facility for access to the FIB-SEM. We thank David Holwell, Raul Fonseca and Associate Editor Christian Ballhaus for helpful and constructive reviews that greatly improved the final paper.

References

Andersen JCO, Rasmussen H, Nielsen TFD, Ronsbo JG (1998) The Triple Group and the Platinova gold and palladium reefs in the Skaergaard Intrusion—Stratigraphic and Petrographic Relations. Econ Geol 93:488–509

Andrews DRA, Brenan JM (2002) The solubility of ruthenium in sulfide liquid; implications for platinum group mineral stability and sulfide melt-silicate melt partitioning. Chem Geol 192:163–181

Ballhaus C, Stumpfl EF (1986) Sulfide and platinum mineralization in the Merensky Reef: evidence from hydrous silicates and fluid inclusions. Contrib Mineral Petrol 94:193–204

Barnes SJ, Fiorentini ML (2008) Iridium, ruthenium and rhodium in komatiites: evidence for iridium alloy saturation. Chem Geol 257:44–58. doi:10.1016/j.chemgeo.2008.08.015

Barnes SJ, Liu W (2012) Pt and Pd mobility in hydrothermal fluids: evidence from komatiites and from thermodynamic modelling. Ore Geol Rev 44:49–58. doi:10.1016/j.oregeorev.2011.08.004

Barnes S-J, Lightfoot PC (2005) Formation of magmatic nickel sulfide deposits and processes affecting their copper and platinum group element contents. Econ Geol 100th Anniv Vol:179–214

Becker H, Horan MF, Walker RJ, Gao S, Lorand J-P, Rudnick RL (2006) Highly siderophile element composition of the Earth's primitive mantle: constraints from new data on peridotite massifs and xenoliths. Geochim Cosmochim Acta 70:4528–4550

Bird DK, Brooks CK, Gannicott RA, Turner PA (1991) A gold-bearing horizon in the Skaergaard Intrusion, East Greenland. Econ Geol 86:1083–1092

Borisov A, Palme H (1997) Experimental determination of the solubility of platinum in silicate melts. Geochim Cosmochim Acta 61:4349–4357

Borisov A, Palme H (2000) Solubilities of noble metals in Fe-containing silicate melts as derived from experiments in Fe-free systems. Am Mineral 85:1665–1673

Boudreau AE, Meurer WP (1999) Chromatographic separation of the platinum-group elements, gold, base metals and sulfur during degassing of a compacting and solidifying igneous crystal pile. Contrib Mineral Petrol 134:174–185

Boudreau AE, Mathez EA, McCallum IS (1986) Halogen geochemistry of the Stillwater and Bushveld Complexes: evidence for transport of platinum group elements by Cl-rich fluids. J Petrol 27:967–986

Campbell IH (1968) The origin of hetradcumulate and adcumulate textures in the Jimberlana Norite. Geol Mag 105:378–383

Campbell IH, Naldrett AJ, Barnes SJ (1983) A model for the origin of the platinum-rich sulfide horizons in the Bushveld and Stillwater Complexes. J Petrol 24:133–165

Canali AC (2014) Solubility of the Assemblage Pt–PtAs in Basalt with Implications for Pt–as complexing and as speciation. Univerity of Toronto, Toronto

Canali AC, Brenan JM (2015) Solubility of the assemblage Pt–PtAs(melt) in basalt with implications for Pt–As complexing and As speciation. In: Geol Ass Canada - Mineral Ass Canada Annual Meeting 2015, Abstracts, p A34039

Edou-Minko A, Grandin G, Campiglio C (2002) Petrologie et geomorphologie dans la region de Kango, Gabon: un grand dyke ultramafique-mafique archeen. J Afr Earth Sci 32:899–918

Finnigan CS, Brenan JM, Mungall JE, McDonough WF (2008) Experiments and models bearing on the role of chromite as a collector of platinum group minerals by local reduction. J Petrol 49(9):1647–1665

Fiorentini ML, Beresford SW, Grguric B, Barnes SJ, Stone WE (2007) Atypical stratiform sulfide-poor platinum-group element mineralisation in the Agnew-Wiluna belt komatiites, Wiluna, Western Australia. Aust J Earth Sci 54:801–824

Fiorentini ML, Barnes SJ, Lesher CM, Heggie GJ, Keays RR, Burnham OM (2010) Platinum-group element geochemistry of mineralized and non-mineralized komatiites and basalts. Econ Geol 105:795–823

Fiorentini ML, Barnes SJ, Maier WD, Burnham OM, Heggie GJ (2011) Global variability in the platinum-group element contents of komatiites. J Petrol 52:83–112

Fonseca ROC, Campbell IH, O'Neill HSC, Allen CM (2009) Solubility of Pt in sulphide mattes: implications for the genesis of PGE-rich horizons in layered intrusions. Geochim Cosmochim Acta. doi:10.1016/j.gca.2009.06.038

Fonseca ROC, Laurenz V, Mallmann G, Luguet A, Hoehne N, Jochum KP (2012) New constraints on the genesis and long-term stability of Os-rich alloys in the Earth's mantle. Geochim Cosmochim Acta 87:227

Godel B (2013) High-Resolution X-ray computed tomography and its application to ore deposits: from data acquisition to quantitative three-dimensional measurements with case studies from Ni–Cu–PGE Deposits. Econ Geol 108:2005–2019. doi:10.2113/econgeo.108.8.2005

Godel BM, Barnes SJ, Barnes S-J, Maier WD (2010) Platinum ore in 3D: insights from high-resolution X-ray computed tomography. Geology 38:1127–1130

Godel BM, Gonzalez-Alvarez I, Barnes SJ, Barnes S-J, Parker P, Day J (2012) Sulfides and sulfarsenides from the Rosie nickel prospect, Duketon greenstone belt, Western Australia. Econ Geol 107:275–294

Godel BM, Barnes SJ, Gurer D, Austin P, Fiorentini ML (2013) Chromite in komatiites: 3D morphologies with implications for crystallization mechanisms. Contrib Mineral Petrol 165:173–189. doi:10.1007/s00410-012-0804-y

Godel B, Rudashevsky NS, Nielsen TFD, Barnes SJ, Rudashevsky VN (2014) New constraints on the origin of the Skaergaard Intrusion Cu–Pd–Au mineralization: insights from high-resolution X-ray computed tomography. Lithos 190–191:27–36. doi:10.1016/j.lithos.2013.11.019

Hanley JJ (2007) The role of arsenic-rich melts and mineral phases in the development of high-grade Pt–Pd mineralization within komatiite-associated magmatic Ni–Cu sulfide horizons at Dundonald Beach South, Abitibi Subprovince, Ontario, Canada. Econ Geol 102(2):305–317

Helmy HM, Ballhaus C, Fonseca ROC, Nagel TJ (2013) Fractionation of platinum, palladium, nickel, and copper in sulfide-arsenide systems at magmatic temperature. Contrib Mineral Petrol 166(6):1725–1737. doi:10.1007/s00410-013-0951-9

Holwell DA, Keays RR (2014) The formation of low-volume, high-tenor magmatic PGE-Au sulfide mineralization in closed systems; evidence from precious and base metal geochemistry of the Platinova Reef, Skaergaard Intrusion, East Greenland. Econ Geol 109(2):387–406. doi:10.2113/econgeo.109.2.387

Karup-Moller S, Makovicky E, Barnes SJ (2008) The metal-rich portions of the phase system Cu–Fe–Pd–S at 1000 degrees C, 900 degrees C and 725 degrees C; implications for mineralization in the Skaergaard Intrusion. Mineral Mag 72(4):941–951. doi:10.1180/minmag.2008.072.4.941

Keays RR, Lightfoot PC (2010) Crustal sulfur is required to form magmatic Ni–Cu sulfide deposits; evidence from chalcophile element signatures of Siberian and Deccan Trap basalts. Mineral Depos 45(3):241

Keays RR, Lightfoot PC, Hamlyn PR (2012) Sulfide saturation history of the stillwater complex, Montana: chemostratigraphic variation in platinum group elements. Mineral Depos 47(1–2):151–173

Kirkham R, Dunn P, Kuczewski A, Siddons D, Dodanwela R, Moorhead G, Ryan C, De Geronimo G, Beuttenmuller R, Pinelli D, Pfeffer M, Davey P, Jensen M, Paterson D, de Jonge M, Kusel M, McKinlay J (2010) The Maia spectroscopy detector system: engineering for integrated pulse capture, low-latency scanning and real-time processing. Proc Aust Inst Phys 1234:240–243

Kogiso T, Suzuki K, Suzuki T, Shinotsuka K, Uesugi A, Takeuchi A, Suzuki Y (2008) Detecting micrometer-scale platinum-group minerals in mantle peridotite with microbeam synchrotron radiation X-ray fluorescence analysis. Goeochem Geophys Geosyst 9:Q03018. doi:10.1029/2007GC001888

Laird JS, Szymanski R, Ryan CG, Gonzalez-Alvarez I (2013) A labview based FPGA data acquisition with integrated stage and beam transport control. Nucl Instrum Methods Phys Res B 306:71–75. doi:10.1016/j.nimb.2012.12.045

Locmelis M, Barnes SJ, Pearson NJ, Fiorentini ML (2009) Anomalous sulfur-poor platinum-group element mineralization in komatiitic cumulates, Mount Clifford, Western Australia. Econ Geol 104:841–855

Lorand J-P, Luguet A, Alard O (2008) Platinum-group elements; a new set of key tracers for the Earth's interior. Elements 4(4):247–252. doi:10.2113/gselements.4.4.247

Maier WD, Barnes SJ, Campbell IH, Fiorentini ML, Peltonen P, Barnes S-J, Smithies RH (2009) Progressive mixing of meteoritic veneer into the early Earth's deep mantle. Nature 460:620–623. doi:10.1038/nature08205

Maier WD, Rasmussen B, Fletcher I, Godel B, Barnes SJ, Fisher L, Yang SH, Huhma H, Lahaye Y (2015) Petrogenesis of the ~2.77 Ga Monts de Cristal Complex, Gabon: evidence for direct precipitation of Pt-arsenides from basaltic magma. J Petrol. doi:10.1093/petrology/egv035

Mathison CI (1987) Pyroxene oikocrysts in troctolitic cumulates; evidence for supercooled crystallisation and postcumulus modification. Contrib Mineral Petrol 97(2):228

McBirney AR, Noyes RM (1979) Crystallization and layering in the Skaergaard intrusion. J Petrol 20:487–554

Mungall JE, Brenan JM (2014) Partitioning of platinum-group elements and Au between sulfide liquid and basalt and the origins of mantle-crust fractionation of the chalcophile elements. Geochim Cosmochim Acta 125:265–289. doi:10.1016/j.gca.2013.10.002

Mungall JE, Naldrett AJ (2008) Ore deposits of the platinum-group elements. Elements 4(4):253–258. doi:10.2113/gselements.4.4.253

Naldrett AJ, Lehmann J, Auge T (1989) Spinel non-stoichiometry and reactions between chromite and closely associated sulphides, with examples from ophiolite complexes. Inst Min Metall, London

Nielsen TFD, Anderson JCO, Holness MB, Keiding JK, Rudashevsky NS, Rudashevsky VN, Salmonsen LP, Tegner C, Veksler IV (2015) The Skaergaard PGE and gold deposit: the result of in situ fractionation, sulphide saturation, and magma chamber-scale precious metal redistribution by immiscible Fe-rich melt. J Petrol 56:643–1676. doi:10.1093/petrology/egv049

Park J-W, Campbell IH (2013) Platinum alloy and sulfur saturation in an arc-related basalt to rhyolite suite; evidence from the Pual Ridge lavas, the eastern Manus Basin. Geochim Cosmochim Acta 101:76

Paterson D, de Jonge MD, Howard DL, Lewis W, McKinlay J, Starritt A, Kusel M, Ryan CG, Kirkham R, Moorhead G, Siddons DP (2011) The X-ray fluorescence microscopy beamline at the australian synchrotron. Proc Aust Inst Phys 1365:219–222

Pina R, Gervilla F, Barnes SJ, Ortega L, Lunar R (2015) Liquid immiscibility between arsenide and sulfide melts; evidence from a LA-ICP-MS study in magmatic deposits at Serrania de Ronda (Spain). Mineral Depos 50(3):265–279. doi:10.1007/s00126-014-0534-3

Prichard HM, Fisher PC, McDonald I, Knight RD, Black AP, Sharp DR, Williams JP (2013) The distribution of PGE and the role of arsenic as a collector of PGE in the Spotted Quoll nickel ore deposit in the Forrestania Greenstone Belt, Western Australia. Econ Geol 108:1903–1922

Ryan CG, Kirkham R, Hough RM, Moorhead G, Siddons DP, de Jonge MD, Paterson DJ, De Geronimo G, Howard DL, Cleverley JS (2010) Elemental X-ray imaging using the Maia detector array: the benefits and challenges of large solid-angle. Nucl Instrum Methods Phys Res A 619:37–43

Ryan CG, Siddons DP, Kirkham R, Li ZY, de Jonge MD, Paterson DJ, Cleverley JS, Kuczewski A, Dunn PA, Jensen M, De Geronimo G, Howard DL, Godel B, Dyl KA, Fisher LA, Hough RM, Barnes SJ, Bland PA, Moorhead GF, James SA, Spiers KM, Falkenberg G, Boesenberg U, Wellenreuther G (2014a) The Maia detector array and X-ray fluorescence imaging system: locating rare precious metal phases in complex samples Proc SPIE 8851. X-Ray Nanoimaging Instrum Methods 8851:88510Q. doi:10.1117/12.2027195

Ryan CG, Siddons DP, Kirkham R, Li ZY, de Jonge MD, Paterson DJ, Kuczewski A, Howard DL, Dunn PA, Falkenberg GU, Boesenberg U, De Geronimo G, Fisher LA, Halfpenny A, Lintern MJ, Lombi E, Dyl KA, Jensen M, Moorhead GF, Cleverley JS, Hough RM, Godel B, Barnes SJ, James SA, Spiers KM, Alfeld M, Wellenreuther G, Vukmanovic Z, Borg S (2014b) Maia X-ray fluorescence imaging: Capturing detail in complex natural samples. J Phys Conf Ser 499:012002

Tomkins AG (2010) Wetting facilitates late-stage segregation of precious metal-enriched sulfosalt melt in magmatic sulfide systems. Geology 38(10):951–954

Wager LR, Brown GM (1968) Layered igneous rocks. Oliver and Boyd, Edinburgh, p 588

Wager LR, Brown GM, Wadsworth WJ (1960) Types of igneous cumulates. J Petrol 1:73–85

Wohlgemuth-Ueberwasser CC, Fonseca ROC, Ballhaus C, Berndt J (2013) Sulfide oxidation as a process for the formation of copper-rich magmatic sulfides. Mineral Depos 48(1):115–127. doi:10.1007/s00126-012-0420-9